Reservoir characterization over the Lille Prinsen and Ivar Aasen fields in the Norwegian North Sea using ocean-bottom-node seismic data — A case study

Satinder Chopra[1], Ritesh Kumar Sharma[1], Mikal Trulsvik[2], Adriana Citlali Ramirez[2], David Went[3], and Bent Erlend Kjølhamar[2]

Abstract

We have developed an integrated workflow for estimating elastic parameters within the Late Triassic Skagerrak Formation, the Middle Jurassic Sleipner and Hugin Formations, the Paleocene Heimdal Formation, and the Eocene Grid Formation in the Utsira High area of the Norwegian North Sea. Our workflow begins with petrophysical analysis carried out at the available wells. Then, model-based prestack simultaneous impedance inversion outputs were derived, and attempts were made to estimate the petrophysical parameters (the volume of shale, porosity, and water saturation) from seismic data using extended elastic impedance. On not obtaining convincing results, we switched over to multiattribute regression analysis for estimating them, which yielded encouraging results. Finally, the Bayesian classification approach was used for defining different facies in the intervals of interest.

Introduction

The Northern North Sea area consists of the Viking Graben running north to south, which is flanked by the Shetland Platform to the west and the Utsira High to the east. The Utsira High is a basement high. Prior to 2007, the Utsira High had almost been dismissed as unprospective, after decades of exploration; however, the discovery of the Edvard Grieg field in 2007 by Lundin Norway was followed by a string of other discoveries, namely, the Ivar Asaen field (discovered by Aker BP in 2008), the Rolvsnes (in 2009), the giant Johan Sverdrup (in 2010), the Apollo (in 2010), and the Solveig (in 2013) fields, all four discovered by Lundin Norway, and the Lille Prinsen field discovered by Equinor in 2018. Thanks to these discoveries, today the Utsira High area is busy with fresh activity.

Lying to the northwest of the large, well-known Johan Sverdrup oil field, the Lille Prinsen field was discovered in the summer of 2018. It is located 200 km west of Stavanger and 5 km northeast of the Ivar Aasen field. The Ivar Aasen field was discovered in 2008 in a water depth of 110 m with the discovery well 16/1-9, which produced oil. The reservoir lies at a depth of 2400 m in the Late Triassic to Middle Jurassic Skagerrak and Sleipner Formations consisting of fluvial sandstones.

Well 16/1-7 drilled in the Ivar Aasen field in 2004 proved the presence of oil in the Mid-Jurassic Hugin and Sleipner sandstone formations. Soon after appraisal well 16/1-11 proved 25 m gas column in the Sleipner Formation and a 32 m oil column in the Skagarrek Formation, without encountering oil-water contact. The oil and gas presence was encountered in the same reservoir intervals as seen in the 2008 discovery well 16/1-9. Although well 16/1-22S subsequently encountered a 3 m oil column in the Skagarrek Formation with no oil-water contact seen, two sidetrack wells, namely, 16/1-22A and 16/1-22B were more productive, with the former striking 55 m and the latter 45 m oil columns in the Skagarrek Formation.

Over the Lille Prinsen field, well 16/1-6S found small amounts of gas, which were not commercially viable. The well was terminated in the Cretaceous. Well 16/1-29S was the discovery well, which encountered 17 m of oil in the clastic reservoir rocks, 30 m of oil and gas in the Eocene Grid Formation (in the form of injectites), 15 m of gas in the Heimdal Formation in the Paleocene with very good reservoir properties, and oil and gas from other thin layers, which added up to an overall 95 m of hydrocarbon pay.

The above description has been summarized in Table 1.

[1]Formerly TGS, Houston, Texas, USA; presently SamiGeo, Calgary, Alberta T3L 1W3, Canada. E-mail: satichop@gmail.com (corresponding author); riteshpes@gmail.com.

[2]TGS, Oslo 0277, Norway. E-mail: mikal.trulsvik@tgs.com; adriana.citlali.ramirez@tgs.com; bent.kjolhamar@tgs.com.

[3]TGS, Woking GU21 5BH, UK. E-mail: david.went@tgs.com.

Manuscript received by the Editor 7 December 2020; revised manuscript received 9 March 2021; published ahead of production 10 May 2021. This paper appears in *Interpretation*, Vol. 9, No. 3 (August 2021); p. 1–17, 26 FIGS., 1 TABLE.

http://dx.doi.org/10.1190/INT-2020-0241.1.

Given the above status for the different wells, it becomes mandatory to understand the spatial distribution of the reservoir and petrophysical properties of the different productive zones in the stratigraphic column of interest. As stated above, these zones comprise the Skagarrek, the Sleipner, the Hugin, the Heimdal, and the Grid Formations. Thus, an exercise was planned for reservoir characterization feasibility analysis, which would encompass the Ivar Aasen and the Lille Prinsen fields and have the well-log curves available for some of the wells mentioned above. This area measured 75 km^2, and its outline is shown in Figure 1 along with the location of the wells.

We begin by explaining the stratigraphic column for the area of interest, followed by the description of the ocean bottom node (OBN) seismic data available. Then, we discuss the workflow planned for the exercise and as we progressed through, what worked for us, and how we addressed some of the issues that came our way.

Geologic setting

The generalized stratigraphic column for the greater Utsira High area is shown in Figure 2.

The metamorphic and intrusive rocks of Caledonian age form the economic basement for much of the North Sea Region. Extensional tectonism, rifting happened during the Carboniferous to Permian during which extrusion of volcanics and deposition of reddish eolian and fluvial sandstone (Rotligendes) took place. This was followed by the deposition of the Middle to Late Permian Zechstein Group consisting of halite, anhydrite, dolomite, and shale.

The Triassic saw a period of accelerated major extension with north–south and northeast–southwest rifting and the formation of rotated fault blocks. The emplacement of the Viking Graben took place during this time giving evidence of subsidence. The Middle to Upper Triassic Skagerrak Formation was deposited in alluvial fans and alluvial plains in a structurally controlled basin. The Middle Jurassic Sleipner Formation is essentially a continental fluvio-deltaic coal-bearing sequence. The overlying Middle Jurassic to Upper Jurassic Hugin Formation was deposited in a shallow marine environment with some continental fluvio-deltaic influence and exhibits higher porosity. The Upper Jurassic Heather Formation overlies the Hugin Formation and represents shales of the Viking Group.

During the Late Jurassic, the largest rifting phase in the North Sea took place with major block faulting followed by erosion and coarse clastic, deltaic sediment supply. The eustatic sea level rise that followed led to transgression and deepwater sedimentation (Ziegler, 1988). In semienclosed basins that had anoxic bottom conditions, thick sequences of organic-rich shale formations got deposited, for example, the Kimmeridgian to Ryazanian Draupne Formation, which is the most important source rock in the North Sea. Mid-Jurassic reservoirs sourced by Kimmeridgian source rocks are to date the most successful play.

The Cretaceous saw the rifting cease and was followed by uniform thermal subsidence into the Tertiary. Uplift of the western platforms, most notably the East Shetland platform, during the Paleocene and early Eocene resulted in deposition of coarse clastic sedi-

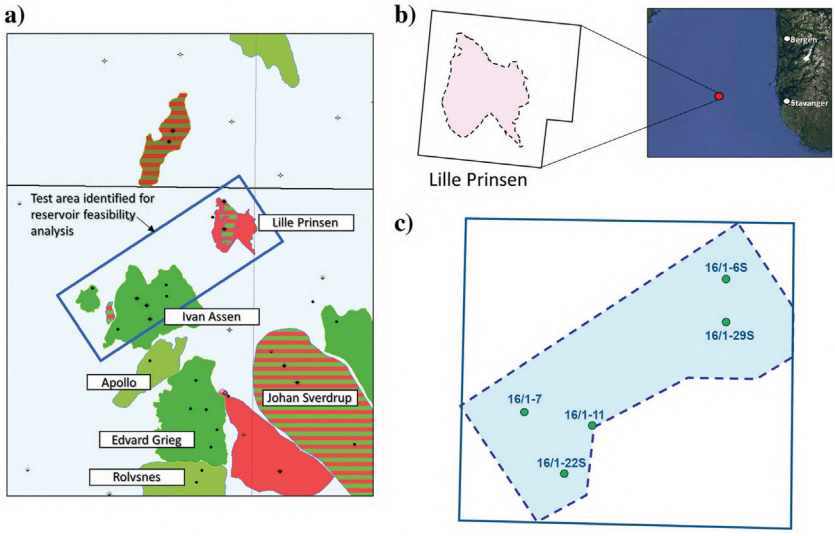

Figure 1. (a) Index map showing the location of the Lille Prinsen and Ivar Aasen fields adjacent to some others in the area and in particular the giant Johan Sverdrup oil field. (b) Location of the Lille Prinsen field with respect to the city of Stavanger. Index map showing the test area identified for reservoir characterization exercise where full-fold OBN seismic data were available.

Table 1 Status of some of the wells in the Utsira High area and falling on the 3D seismic volume.

Formation	W 16/1-9	W16/1-7	W16/1-11	W16/1-22S	W16/1-22A	W16/1-22B	W16/1-6S	W16/1-29S
Grid	—	—	—	—	—	—	—	Oil/gas
Heimdal	—	—	—	—	—	—	—	Gas
Hugin	—	Oil	—	—	—	—	—	—
Sleipner	Oil	Oil	Oil	—	—	—	—	—
Skagerrak	Oil	—	Oil	Oil	Oil	Oil	—	—

ments in the basin in the form of deltas and basinal fans. The Paleocene and Eocene fans formed reservoir targets in the Utsira High area.

Availability of the seismic data and workflow adopted

Besides the earlier 2D seismic, the Utsira High area has been covered with different generations of 3D streamer seismic, ocean-bottom cable, split spread with blended sources, and multiazimuth surveys. More recently, ocean-bottom seismic surveys have gradually demonstrated better illumination of the subsurface through long offsets (good for multiple attenuation and undershoot imaging), wide azimuths (useful for better imaging and resolution of complex structures), and higher signal-to-noise ratios through dense sampling and high fold. Ocean-bottom surveys tend to be expensive but are increasingly seen as cost effective.

With all of the above-stated advantages, OBN technology is now available, is cost effective, productive, and hence economical. It is becoming a system of choice for many reservoir characterization and monitoring projects. In 2018 and 2019, partners TGS and AGS acquired a 1584 km^2 3D multiclient survey over the Utsira High. The data were acquired in two phases and merged into a single volume after processing in 2020. To extract more value out of the regional product, it was decided to carry out a reservoir characterization and fluid fill feasibility analysis which, if promising, could be used in field development, production, and near-field exploration. A 75 km^2 test area was identified that encompassed the Lille Prinsen and Ivan Aasen fields. Well logs from six wells were provided for carrying out the reservoir characterization exercise with the objective of spatial distribution of reservoir and petrophysical properties in the zones of interest, namely, the Skagerrak, the Sleipner, the Hugin, the Heimdal, and the Grid Formations as described earlier.

On closely examining the well curves in the available wells, it was found that the Grid sandstones in the form of injectites and Heimdal sandstones when water-bearing are hard with respect to the shales. Similarly, Sleipner sandstones when water-bearing are found to be only slightly harder and slightly softer when hydrocarbon-bearing than the Heather Shale. The well curves exhibit higher velocities and lower densities for the sandstones and an opposite response for shaly formations. Because the higher velocity and lower density counteract each other, the acoustic impedance (the product of velocity and density) is not a reliable indicator of lithology in these formations. The only exception is seen in well 16/1-7. Therefore, it was challenging to characterize these multiple formations simultaneously with poststack impedance inversion.

For multiple zones of interest, the main objectives are to differentiate among different lithologies and their fluid fill distribution. Accordingly, a plan was drawn up for addressing the multizone characterization objective with the following sequence:

1) perform petrophysical analysis for all the available wells and use that data to study property distribution patterns for lithology, reservoir quality, and fluid discrimination in the crossplot space for different intervals of interest
2) precondition the OBN seismic data to produce inversion-ready angle gathers (or partial angle stacks)
3) perform amplitude-variation-with-offset (AVO) analysis for the AVO intercept and gradient, and prestack simultaneous impedance inversion for absolute P-impedance, absolute S-impedance, and V_P/V_S
4) use extended elastic impedance inversion for the determination of petrophysical properties, such as porosity (φ), volume of clay (V_{cl}), and water saturation (S_w)
5) if step 4 does not work, we explore an alternative. The alternative that we adopted was multiattribute regression analysis for obtaining volume of clay, porosity, and water saturation.

Petrophysical analysis on available well-log data

The well logs available for this study were put through a detailed petrophysical analysis, which provided the volume fraction of individual minerals, such as V_{clay}, V_{sand}, and $V_{carbonate}$, along with the estimation of porosity and water saturation. Having all of these curves, crossplot matrix analysis was carried out in which pairs of attributes, which could eventually be derived from seismic data, were crossplotted, and color coded with the property of interest (φ, V_{cl}, and S_w). Although the impact of water saturation on attributes which could eventually be derived from seismic data was not straightforward, it was apparent that P-imped-

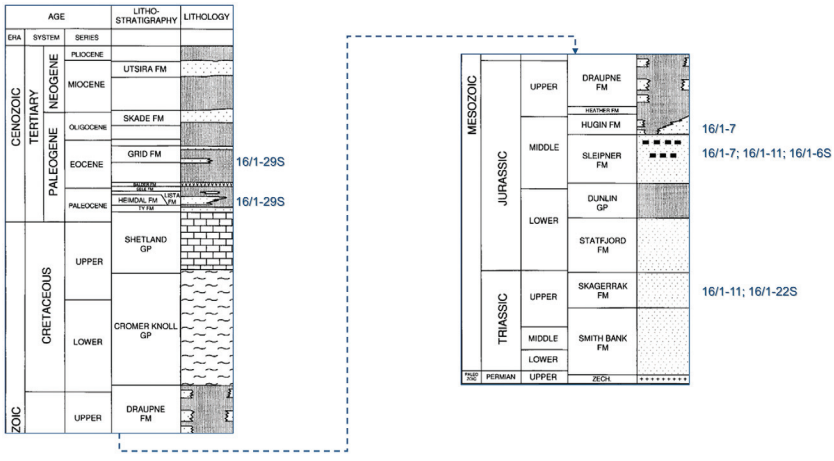

Figure 2. Lithostratigraphy of the greater Utsira High area. The Upper Jurassic Draupne and Heather Formations are the main source rocks for oil and gas. Modified from Isaksen and Ledje (2001).

ance and V_P/V_S could be used to extract information about the main lithofacies (shale, sand, and carbonate) and porosity. This observation suggested the application of prestack impedance inversion, for which the first step is the well-to-seismic ties and is discussed next.

Well-to-seismic ties

Any seismic interpretation exercise begins with tying seismic data with the available well-log control. The edited well-log curves (shown in red in Figure 3) were smoothed (shown in blue) by using a running average smoother. For generating a synthetic seismogram, the wavelet was extracted from the seismic data statistically. The generated synthetic seismograms were compared with the seismic traces at the well locations for the available wells. Figure 3 shows such a representative correlation for well 16/1-22S. The synthetic seismogram (the traces in blue) is shown correlated with the seismic traces in red, and the correlation coefficient between them was observed to be 0.806, which is reasonably good.

The correlation coefficient for the other wells was also found to be good (in the range of 62%–81%), as seen on the arbitrary line extracted from the seismic data volume and passing through four wells as shown in Figure 4. The trajectory of the arbitrary line is shown on the base map shown in the inset.

Preconditioning of prestack seismic data

The available prestack seismic data were carefully conditioned to ensure that the amplitudes were preserved such that their variation with offset/angle of incidence can be used for quantitative interpretation. The seismic gathers were put through processes, such as muting, supergathering (3×3), band-pass filtering, random noise filtering, and trim statics, and difference plots were taken at each step to ensure that no seismic signal was distorted or attenuated.

A useful quality control during preconditioning of prestack seismic data is to ensure that the AVO/angle of incidence remains unchanged, and how the different reflection events on the processed gathers compare with the modeled reflection events from well logs. To accomplish this, gathers were modeled at well locations with shear sonic curves available and compared with equivalent gathers before and after preconditioning. As shown in Figure 5, the modeled elastic gather at well location 16/1-7 is shown compared to the real processed seismic gather before and after preconditioning. The high amplitudes on the far offsets (Figure 5a and 5b) are the reflection amplitudes originating from beyond the critical angles of incidence. Such amplitudes were muted as shown in Figure 5c. In Figure 5d, we show the variation of amplitude as a function of the angle of incidence at a reflection event close to 1800 ms on the modeled gather (indicated by the red bar), the input gather (the blue bar), and the preconditioned gather (the pale yellow bar). We note that the scattering of the amplitude values after preconditioning is reduced, but the overall gradient remains the same, which enhanced our confidence in following adequate steps for data conditioning.

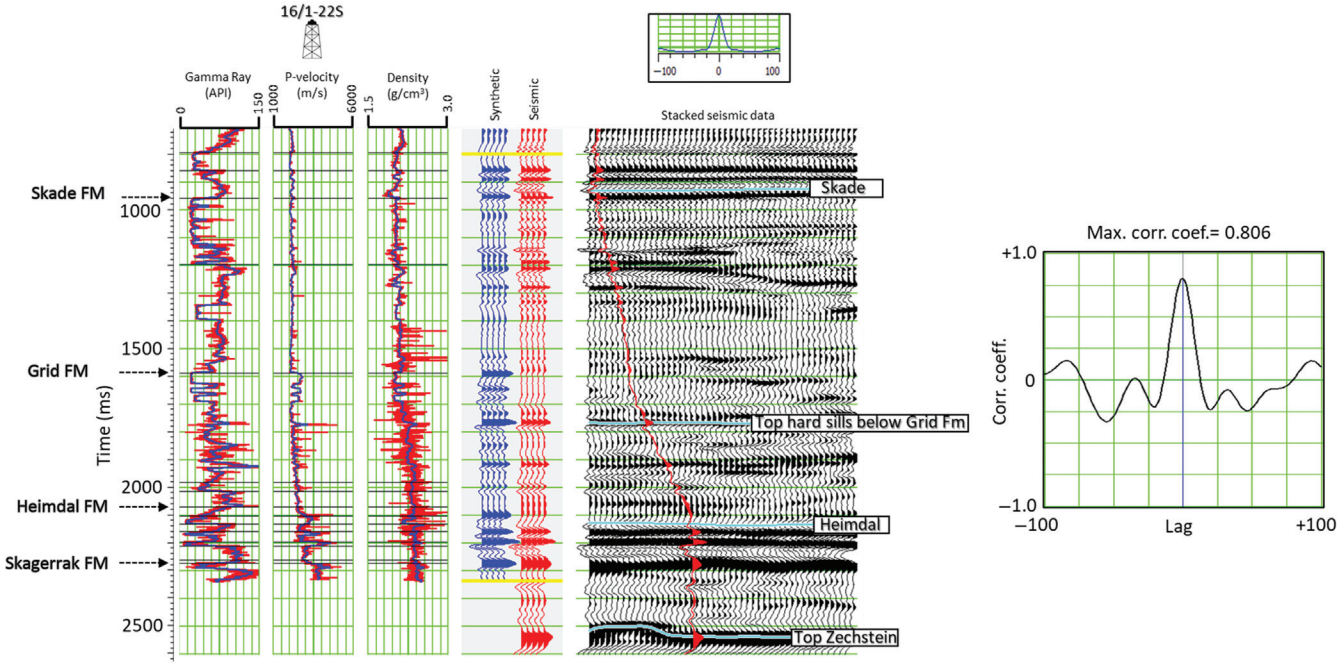

Figure 3. Well-to-seismic correlation for well 16/1-22S. The input well-log curves are shown in red, and their smoothed versions are in red. The wavelet used for the generation of the synthetic trace was extracted from the seismic data using a statistical process, and it is shown on top of the seismic segment. The generated synthetic traces are in blue, and they are shown correlated with the equivalent seismic traces in red. A correlation coefficient of 0.806 is noticed between the two (data courtesy of TGS and AGS, Norway).

Offset-to-angle transformation

Because prestack simultaneous impedance inversion is performed in the time-incidence angle domain, we need to transform the seismic gathers from offset to the angle of incidence domain. For this purpose, the following relationship given by Walden (1991) is used:

$$\mathrm{Sin}\,\theta = \frac{V_{\mathrm{int}} x}{V_{\mathrm{NMO}}^2 t} = \left(\frac{V_{\mathrm{int}}}{V_{\mathrm{smooth}}}\right) \frac{x}{\sqrt{x^2 + (V_{\mathrm{smooth}} t_0)^2}}, \quad (1)$$

where x is the source-receiver offset and V_{int} is the interval velocity obtained from V_{smooth}, which is the spatially varying velocity derived by smoothing the stacking velocities over a receiver cable length (Mukhopadhaya and Mallick, 2011).

As can be seen from the above relationship, velocity plays an important role in domain conversion. Thus, a reliable velocity model is desired for extracting meaningful information from AVO analysis or simultaneous inversion.

Velocity model building

For the purpose mentioned above, either the seismic velocity field derived from processing can be used, or a

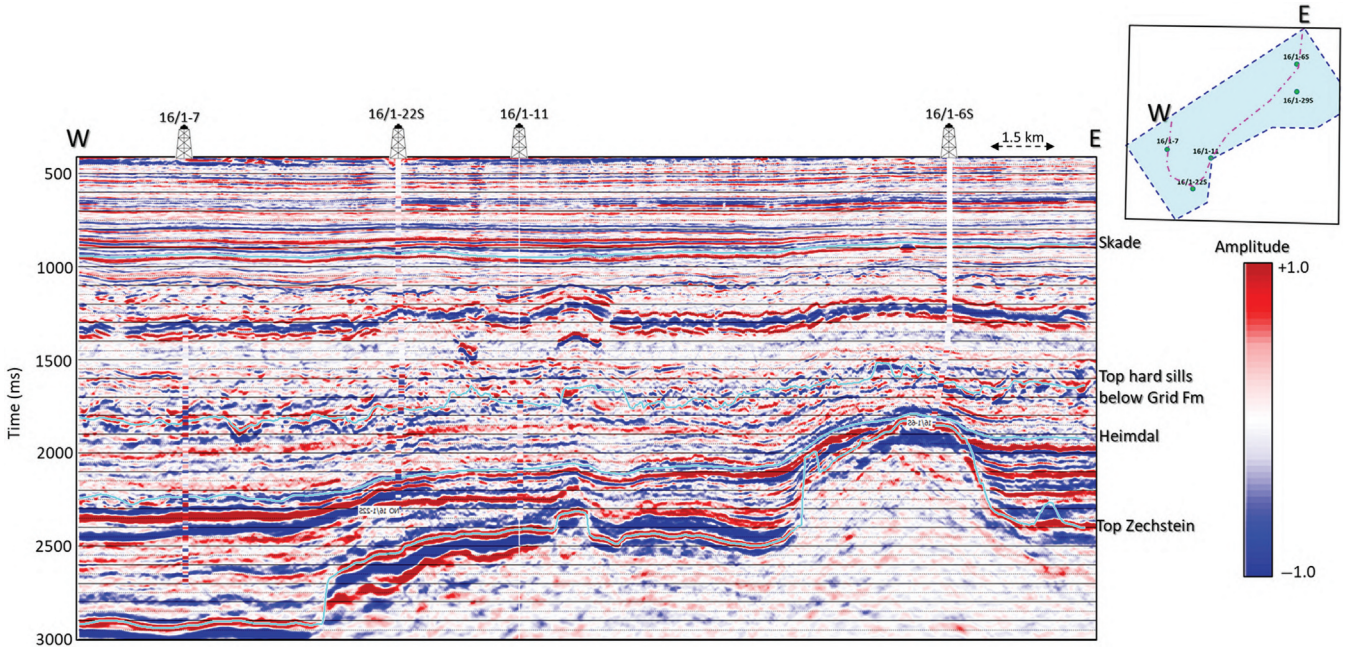

Figure 4. An arbitrary line passing through different wells as indicated extracted from the stacked seismic volume. The synthetic traces at the well locations are interfixed on the section, and a reasonable correlation is noticed (data courtesy of TGS and AGS, Norway).

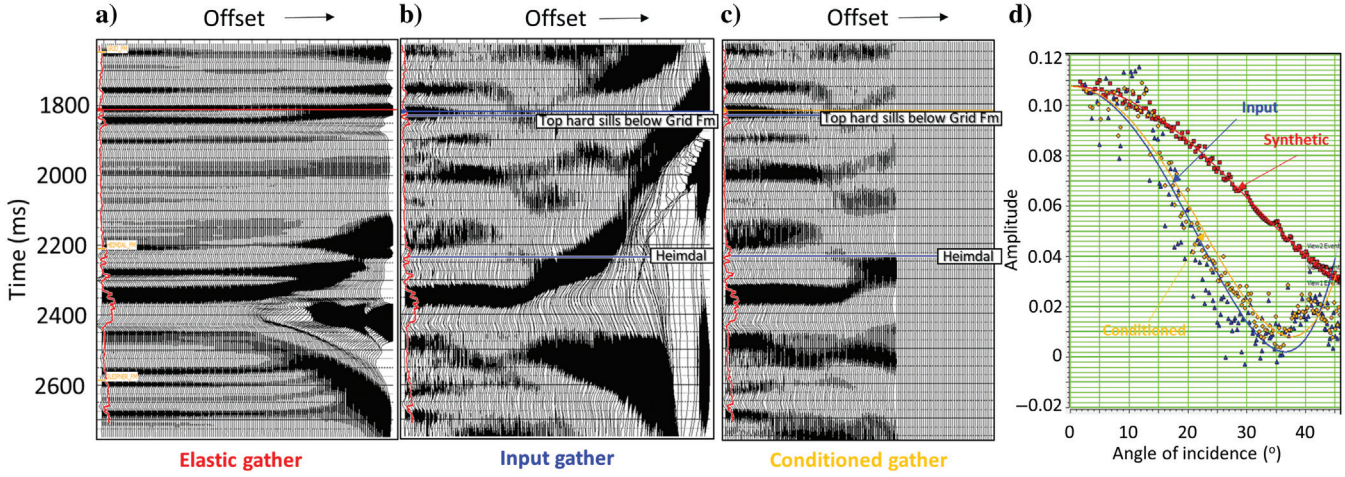

Figure 5. (a) Modeled elastic gather at well 16/1-7 generated using the same geometry as the field seismic data. (b) The equivalent input gather at the location of well 16/1-7 and (c) the same gather in (b) after preconditioning. Note the enhancement in the signal-to-noise ratio of the data. The variation of the amplitudes as a function of angle of incidence for the three gathers shown in (a-c) (data courtesy of TGS and AGS, Norway).

well-driven velocity field can be generated. Although the seismic velocity provides spatial variation, it falls short of capturing detailed information temporally. During processing, seismic velocities are usually picked keeping an increasing trend in mind, so that the interval velocities obtained after conversion and smoothing also exhibit a smooth trend with increasing time. When such an interval velocity field was used for the offset-to-angle transformation and overlaid in color on the seismic offset gathers, even in the presence of sharp contrasting interfaces in the subsurface, the angles of incidence did not exhibit sharp changes. In addition, it is not guaranteed that seismic velocities would be horizon consistent and would match with the measured well-log curves. However, the well-driven velocity field exhibits detailed information and is horizon consistent, so it is preferred for domain conversion. The usual practice for the generation of a well-driven velocity model is to smooth the available sonic well-log curves and use one or more of those curves for the generation of the velocity field using extrapolation/interpolation. Such interpolation/extrapolation of velocity values is usually guided by the picked horizon boundaries. In cases in which more than one well is used for model building, usually an inverse distance weighted scheme or a process such as kriging is used. Such schemes could produce artifacts in the form of artificial tongues of sharp impedance changes that may not be geologic and thus should be used with caution (Chopra et al., 2017).

It may be appropriately mentioned here that the accuracy of well-driven velocity model depends on the number of wells used and the condition of horizons used in the analysis. For a geologic scenario exhibiting monotonous facies with flat structures where horizons are easy to track on seismic data, the well-driven velocity field may work well. However, for our area of interest, a significant spatial variation of velocity was evident and due to the complex structure, especially at the basement, most of the horizons were not conveniently pickable over the whole seismic volume. Therefore, it was challenging to build a reliable well-driven velocity model, which honors well data and captures the spatial variation without introducing any artifacts associated with interpolation/extrapolation. Besides, such a velocity model should not be vulnerable to misinterpretation. Thus, an alternative approach for velocity-model building, similar to the one suggested by Ray and Chopra (2016) that uses the well-log data and seismic data for building a low-frequency model, was followed. In their workflow, first a velocity field is generated using a single well, and then the target log is modeled as its linear combination with seismic-driven velocity and

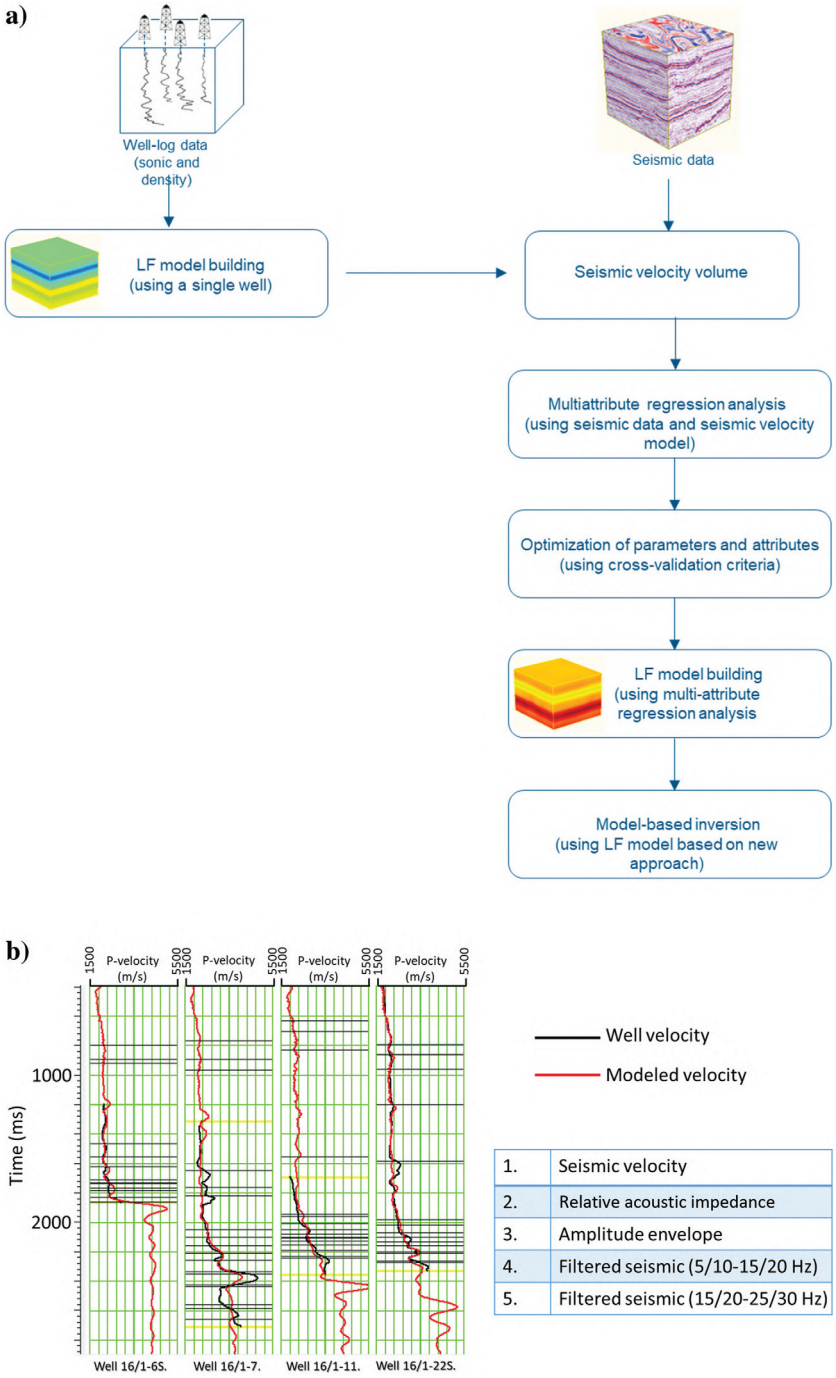

Figure 6. (a) Workflow for generating the low-frequency model using multiattribute regression. (b) Cross-validation analysis with the use of multiple attributes.

other attributes. This modeling yields a series of linear equations, which are solved for obtaining a linear weighted sum of the input seismic attributes in such a way that the error between the predicted and the target log is minimized in a least-squares sense (Chopra et al., 2018).

Knowing the limitations of a single well in capturing the spatial variation of the velocity and challenges in tracking seismic horizons, it was decided not to use an initial model generated with well data. Instead, the seismic velocity model was selected for being updated with the help of multiattribute analysis because it was found to be smoothly exhibiting the lateral subsurface geologic trend. By doing so, an attempt was made to build an integrated velocity model that would honor the well-log data as well as the spatial variation of the seismic velocity. Besides the seismic velocity model, the other seismic attributes used in multiattribute analysis were the relative acoustic impedance, amplitude envelope, and two filtered versions of the input seismic data (5/10–15/20 and 15/20–25/30 Hz) (Figure 6a). The correct number of attributes (four in this case) was determined by the cross-validation method (Hampson et al., 2001). In this method, one well at a time is excluded from the training set and the prediction error is calculated at that well. This process is repeated as many times as there are wells, each time leaving out a different well. If the correlation between the existing and the predicted attributes is high, which happened to be the case, there is more confidence in the analysis (Chopra et al., 2017, 2018). The cross-validation analysis for the different wells is shown in Figure 6b. On obtaining a satisfactory analysis, the integrated velocity volume was generated. Figure 7 shows an arbitrary line section from this volume passing through different wells with the seismic data overlain. Notice how well the final integrated velocity model exhibits the spatial as well as temporal variations consistent with the overlaid well-log curves. Although the integrated velocity model is following most of the horizons, it is not sensitive to misinterpretation of interpreted horizons, which lends confidence in using this velocity field for the angle of incidence computation. In Figure 8, we show the angle information overlaid on conditioned gathers around well 16/1-7 computed using the integrated velocity model. Although the maximum angle of incidence that can be used for AVO analysis or simultaneous inversion seems to be at approximately 49° along a few strong seismic events, it is less than 35° (Figure 8) otherwise. Consequently, the quality of the far-angle stack required for density estimation could be questionable.

After transforming the conditioned offset gathers into angle gathers, the next step is to perform AVO analysis and simultaneous inversion.

AVO analysis

Once the angle gathers are generated, there are different ways of estimating AVO attributes such as the intercept, gradient, P- and S-reflectivities, and other attributes derived from them. All of these options were used and analyzed. However, for the sake of brevity, they are ex-

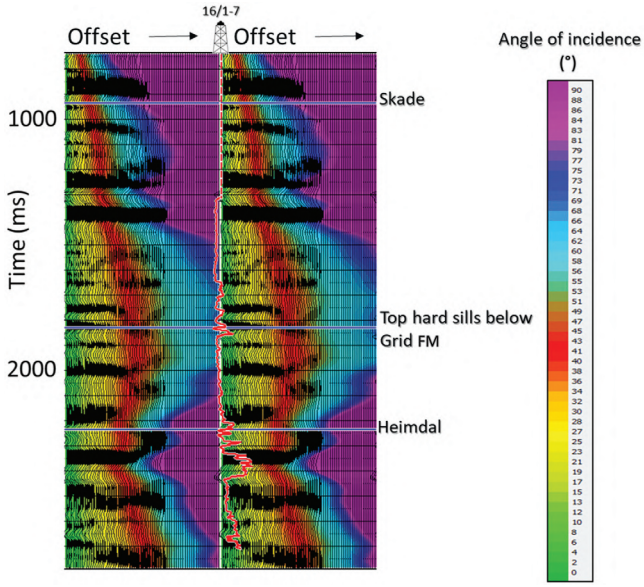

Figure 8. Angle information overlaid on conditioned gathers when the integrated velocity model is used. Sharp changes in the angle of incidence are seen at prominent interfaces as expected. The range of the usable angle of incidence is seen to be 49° at the prominent horizons, but it is much less at others (data courtesy of TGS and AGS, Norway).

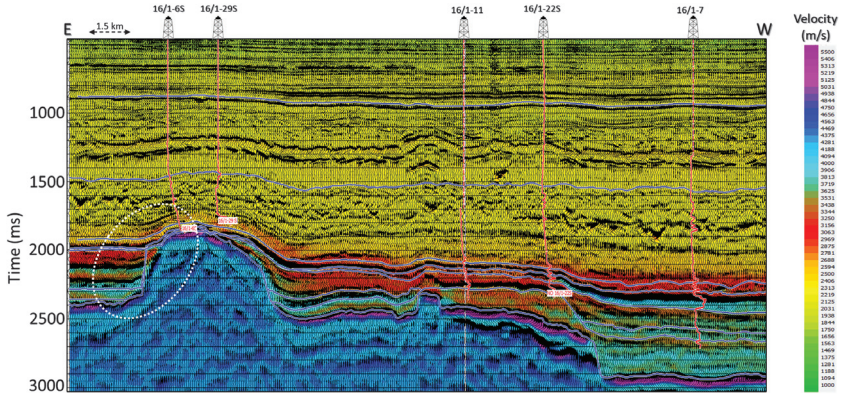

Figure 7. Integrated velocity model section along an arbitrary line with the seismic data overlain. Although the temporal and spatial variations seem to be captured, the final velocity model is not vulnerable to interpreted horizons highlighted with the dotted ellipse (data courtesy of TGS and AGS, Norway).

cluded here because all of these parameters provide qualitative information associated with a particular interface whereas we are more interested in interval properties for quantitative interpretation. Therefore, simultaneous inversion was preferred and is discussed next.

Prestack simultaneous impedance inversion

The inversion process begins with the low-frequency models of P-impedance, S-impedance, and density, which are used to generate the synthetic angle gather when they are convolved with angle-dependent wavelets. These model impedance values are then iteratively tweaked in such a manner that the mismatch between the modeled angle gather and the real angle gather is minimized in a least-squares sense. Thus, it is essential to generate reliable low-frequency models of impedances. Knowing that a strong correlation usually exists between velocity and impedance, which happened to be the case for our area of interest, the integrated velocity volume discussed earlier got transformed into impedance volumes.

For the seismic data at hand, because the frequency content was found to be low (Figure 9b), it was expected to create problems in identifying individual intervals of our interest because their thickness seems to be lower than the seismic resolution. Usually, in such cases, the basic output attributes lack the resolution and thus any rock property attributes computed therefrom also suffer. In view of this, it was decided that the available seismic data be spectrally balanced before putting them through simultaneous impedance inversion. The general workflow for prestack simultaneous impedance inversion, including the desired spectral balancing step, is shown in Figure 9a. We used the amplitude-friendly spectral balancing approach demonstrated by Marfurt and Matos (2014) and Chopra and Marfurt (2016). In this method, seismic data are first decomposed into time-frequency spectral components. Then, the power of the spectral magnitude, $P(t,f) = m(t,f)^2$, is spatially averaged over all the traces ($j = 1, \ldots, K$) in the data volume and in the given time window, which yields a smoothed average power spectrum, given by $P_{\text{avg}}(t,f)$. The peak of the average power spectrum at time t may be defined as $P_{\text{peak}}(t) = \max_f[P_{\text{avg}}(t,f)]$. Using these definitions, the flattened magnitude spectrum is computed as

$$m_j^{\text{bal}}(t,f) = \left[\frac{P_{\text{peak}}(t)}{P_{\text{avg}}(t,f) + \varepsilon P_{\text{peak}}(t)}\right]^{\frac{1}{2}} m(t,f), \qquad (2)$$

where ε is the prewhitening parameter. A conservative value would be $\varepsilon = 0.04$. For larger surveys that exhibit a statistically more robust average spectra, one might use values of $\varepsilon = 0.01$ for broadening the spectrum. However, as is the case with any such filter, the interpreter needs to be cautious if the aggressive spectral balancing by the method introduces ringing in the data. Such spectral balancing is amplitude friendly because a single time-varying operator is applied to the entire data volume (Chopra and Marfurt, 2016).

In Figure 10, we show the correlation of the synthetic seismogram with the seismic data before and after spec-

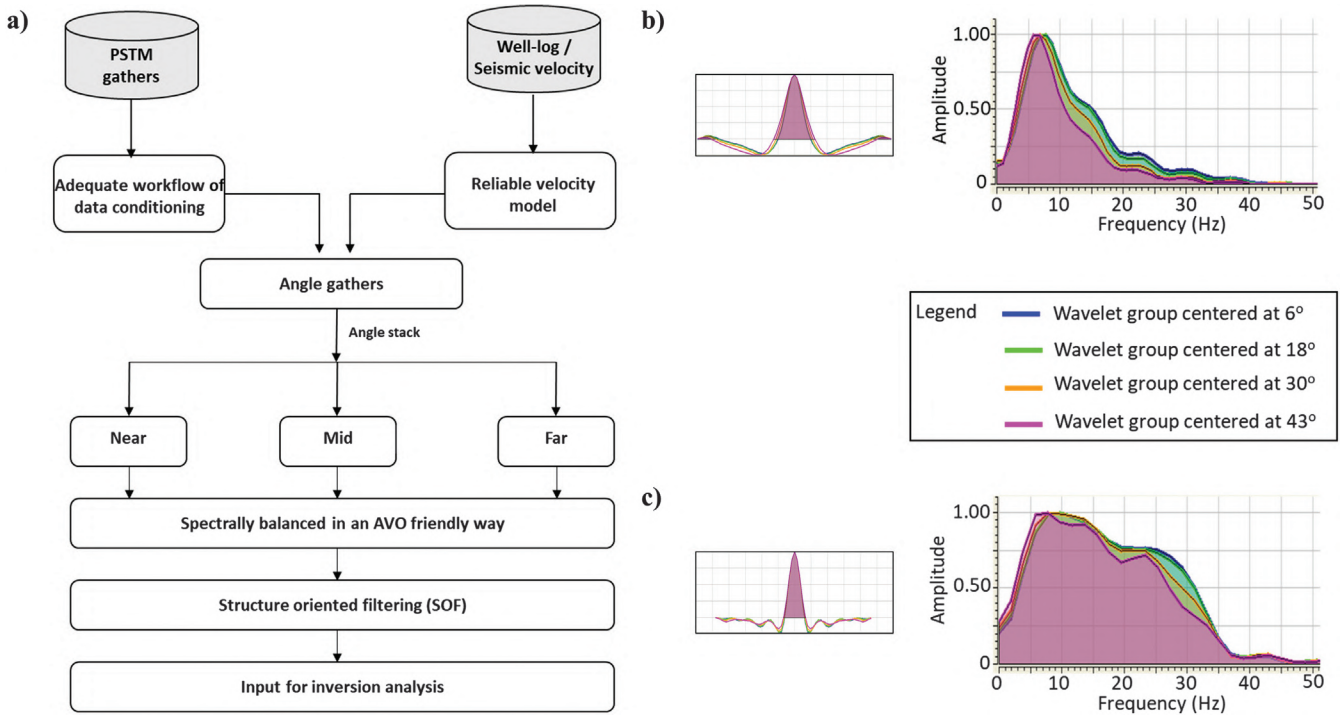

Figure 9. (a) Workflow used for performing simultaneous impedance inversion using spectral balancing and structure-oriented filtering of the data. Wavelets extracted from the different angle stack volumes and their frequency spectra (b) before and (c) after spectral balancing.

tral balancing for well 16/1-7. Note that the correlation coefficient increases from 0.779 to 0.826, which is encouraging. Again, to check on the amplitude variation with angle, we pick amplitudes along an event on the angle gathers comprising the near-, mid-1, mid-2, and far-angle traces with a red bar on the gather before spectral balancing and with a blue bar after balancing. These amplitudes are then plotted as a function of the angle of incidence as shown in Figure 11. Note that the amplitude variation trends do not change, even though the amplitude values are different after spectral balancing, which is expected.

The equivalent wavelets extracted from the same time window before and after frequency balancing are shown in Figure 9b and 9c. Prestack simultaneous impedance inversion carried out with these wavelets and the balanced near-, mid-1, mid-2, and far-angle stacks yield higher resolution and thus lead to more accurate interpretation. In Figure 12, we show an arbitrary line from the P-impedance and V_P/V_S volumes obtained after balancing of the near-, mid-1, mid-2, and far-angle stacks. Note the crisper look of the events and their better standout seen on the sections, which was not the case when angle stacks were used without spectral balancing. Thus, the spectrally enhanced angle gathers were then used in the prestack simultaneous impedance inversion process, and the P- and S-impedance attributes were obtained as the products therefrom.

Then, we crossplot the inverted P-impedance versus the inverted V_P/V_S as shown in Figure 13a for the arbitrary line passing through the indicated wells. After enclosing the cluster points in three different polygons suspected to be exhibiting shale, sand, and carbonate lithologies, and backprojecting on the vertical section as shown in Figure 13b, the individual lithologies can be seen at different levels in gray (shale), yellow (sand), and blue (carbonate).

Thus, by adopting a workflow that entails the generation of P-impedance, and S-impedance attributes and examining them, we can interpret the lateral variation in the lithologies. However, such a classification is a qualitative way of extracting information about different lithologies. To perform quantitative interpretation,

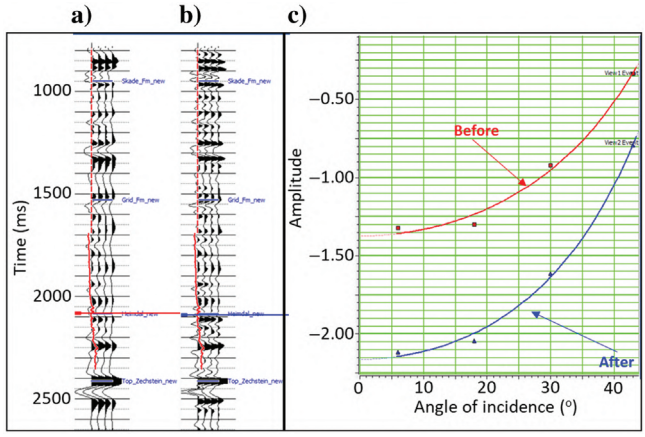

Figure 11. The AVO gradient analysis carried out on gathers (a) before and (b) after balancing at well 16/1-11 is shown in (c) along reflection events indicated by the red and blue bars. Note that the amplitude trends have not changed after spectral balancing (data courtesy of TGS and AGS, Norway).

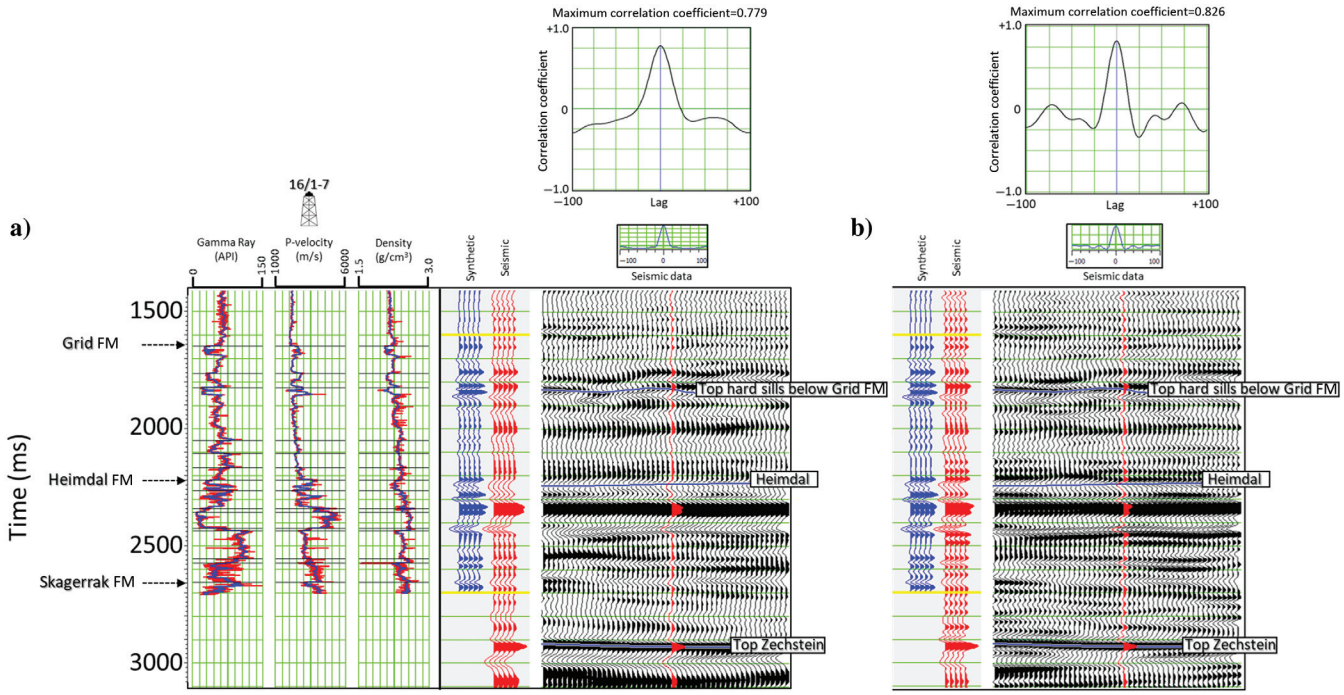

Figure 10. Well-to-seismic tie with (a) input stack data and (b) input stack data after spectral balancing. The frequency content seems to have increased after spectral balancing (data courtesy of TGS and AGS, Norway).

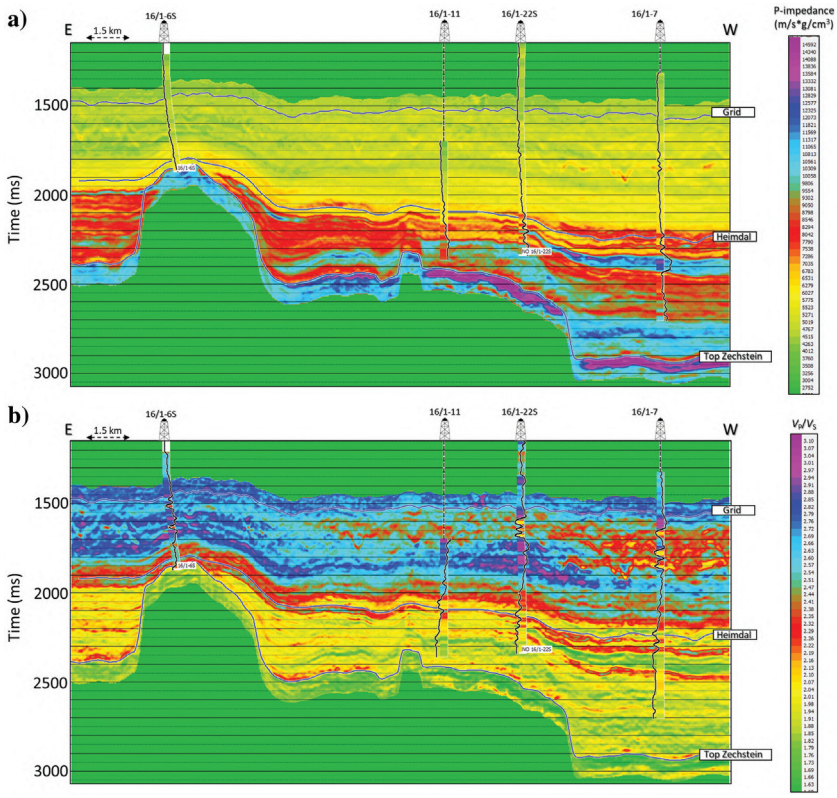

Figure 12. Inverted (a) P-impedance and (b) V_P/V_S sections along the arbitrary line passing through the indicated wells after simultaneous inversion carried out after spectral balancing of angle stack data (data courtesy of TGS and AGS, Norway).

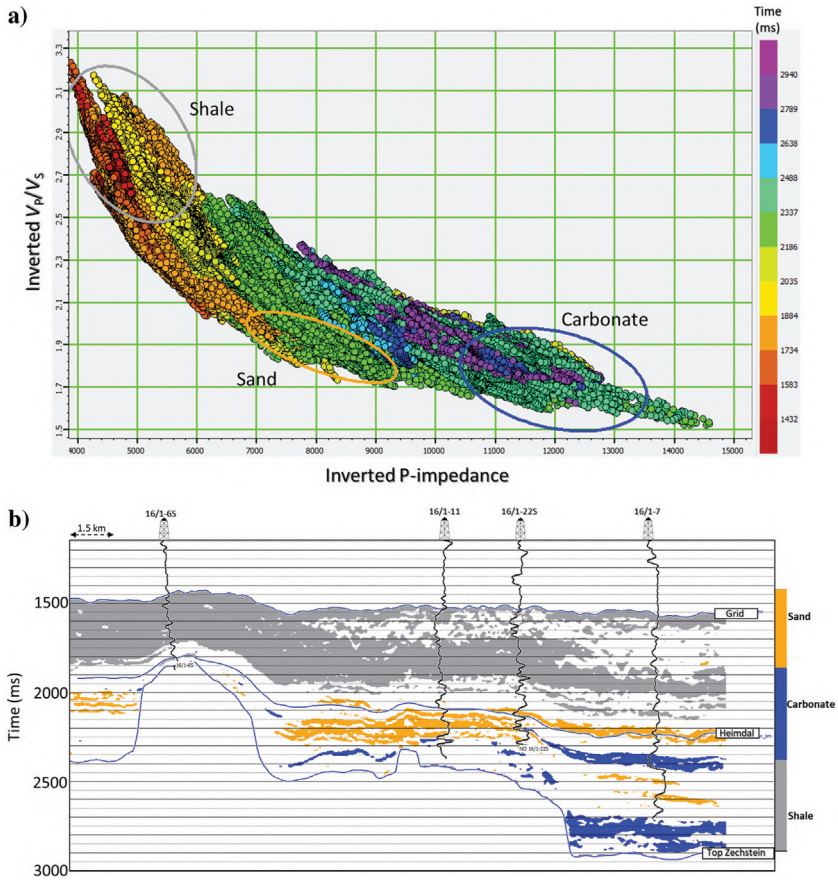

Figure 13. (a) Crossplot of the inverted P-impedance versus V_P/V_S ratio along the arbitrary line after spectral balancing. (b) Back-projection of the datapoints enclosed in the three polygons on the crossplot representing the shale, sand, and carbonate lithologies on the vertical arbitrary line section (data courtesy of TGS and AGS, Norway).

we take this exercise forward to gauge more information in terms of fluid and the uncertainty associated with the computed fluid/lithology attributes.

Extended elastic impedance application

Extended elastic impedance (EEI) is a useful technique for the determination of elastic and petrophysical parameters of interest, and thus was adopted in our analysis. Connolly (1999) introduces elastic impedance as a generalization of the acoustic impedance for variable angles of incidence, which in turn allows the inversion of nonzero offset seismic data for fluid and lithology prediction. But as the elastic impedance approach considers the angles of incidence in the narrow 0°–30° range (values taken by $\sin^2\theta$ in the equation $R(\theta) = A + B\sin^2\theta$), it cannot predict some of the rock properties. Whitcombe et al. (2002) attempt to get over this limitation by making a variable change in that the $\sin^2\theta$ term is replaced with $\tan\chi$. By doing so, the chi angle range is now extended from −90° to +90°. Although many of these angles are beyond the physically observable range of the angles of incidence, this change allows for the computation of impedance at these angles. As the authors demonstrate, the extended elastic impedance at particular values of angle χ is found to correlate with some petrophysical reservoir properties (water saturation, porosity, and volume of clay) as well as elastic properties (bulk modulus, lambda, mu, etc.) which are usually sought for reservoir characterization. A salient point that may be borne in mind, though, is that the new variable (χ) is not the actual angle of incidence but may be considered as an independent variable that is used for computing the extended elastic impedance.

Because EEI numerically transformed impedances are correlated with desirable V_{clay}, and effective porosity log curves for different values of the chi angles, the correlation coefficients are plotted for the four different wells in different colors as shown in Figure 14. We notice that there is no single maxima indicated by the positive correlation coefficients for V_{clay} (Figure 14a); similarly, there is no single minima seen on the negative correlation coefficients for porosity (Figure 14b) among the different wells. The values of the singular angles for these properties allow their determination from seismic data through the application of Zoeppritz equations on seismic angle gathers. We decided to take an average value of χ for the two properties and go ahead with their computations and check on their prediction accuracy. In Figure 15a, we show a comparison of the scaled V_{clay} curve (red) computed via EEI with the V_{clay} curve (blue) generated using petrophysical analysis for well 16/1-7. Note the large mismatches in most of the intervals of interest. A similar comparison for well 16/1-22S is shown in Figure 15b, which again exhibits unacceptable mismatches in the different intervals of interest. On crossplotting EEI computed V_{clay} curves with similar petrophysical curves for all four wells, a poor correlation (approximately 15%) was noticed. Consequently, we abandoned this computation and decided to proceed with the multiattribute analysis for these properties, which we describe next.

Multiattribute analysis for the computation of volume of clay, porosity, and water saturation

Multiattribute regression analysis has been applied in various geophysical problems (Hampson et al., 2001; Leiphart and Hart, 2001), and it has also been described in the previous section on generation of the low-frequency model. In such an approach, a nonlinear relationship is determined between the available seismic attributes and the desired petrophysical property at the location of a well. The determined relationship is then used to predict the desired property away from the well control. In the case at hand, first the multiattribute regression analysis was used to predict the volume of clay (V_{clay}) volume. The available input attributes were the

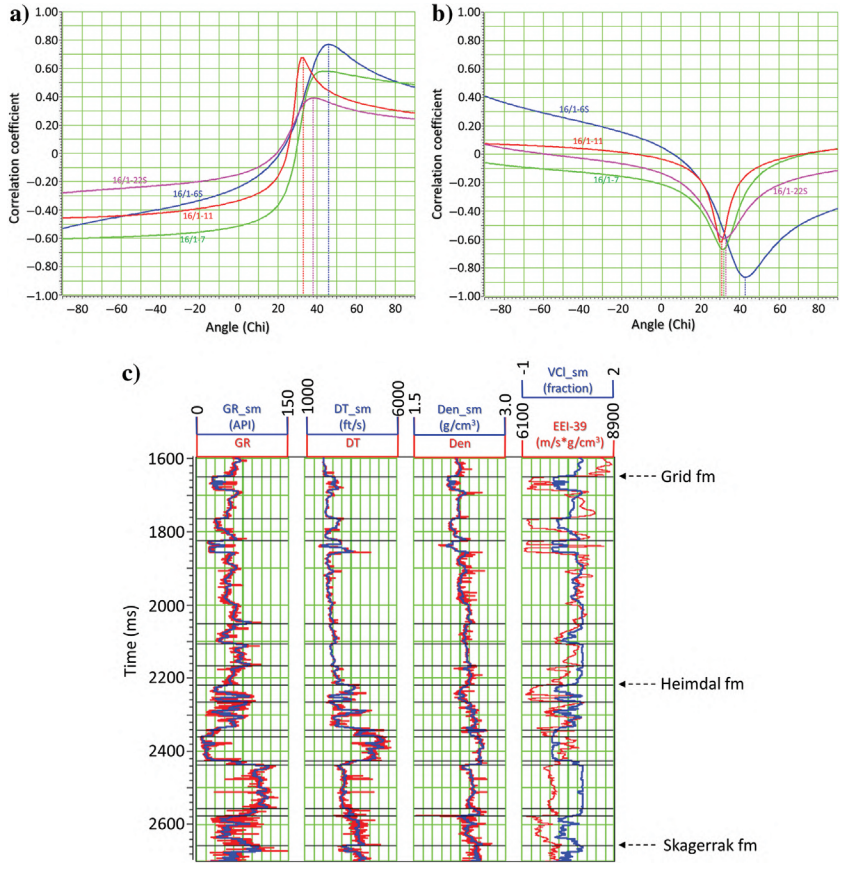

Figure 14. The χ angle estimation for (a) V_{clay} and (b) porosity. (c) Comparison of EEI_39 and V_{clay} at well 16/1-7.

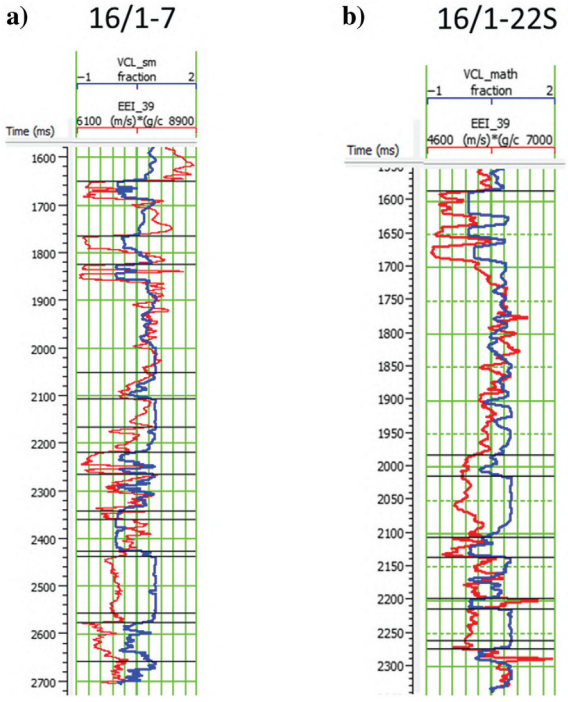

Figure 15. Comparison of predicted V_{clay} using extended elastic impedance (red) and V_{clay} curve obtained through petrophysical analysis (blue) for wells 16/1-7 and 16/1-22S. Significant mismatches are seen in many intervals.

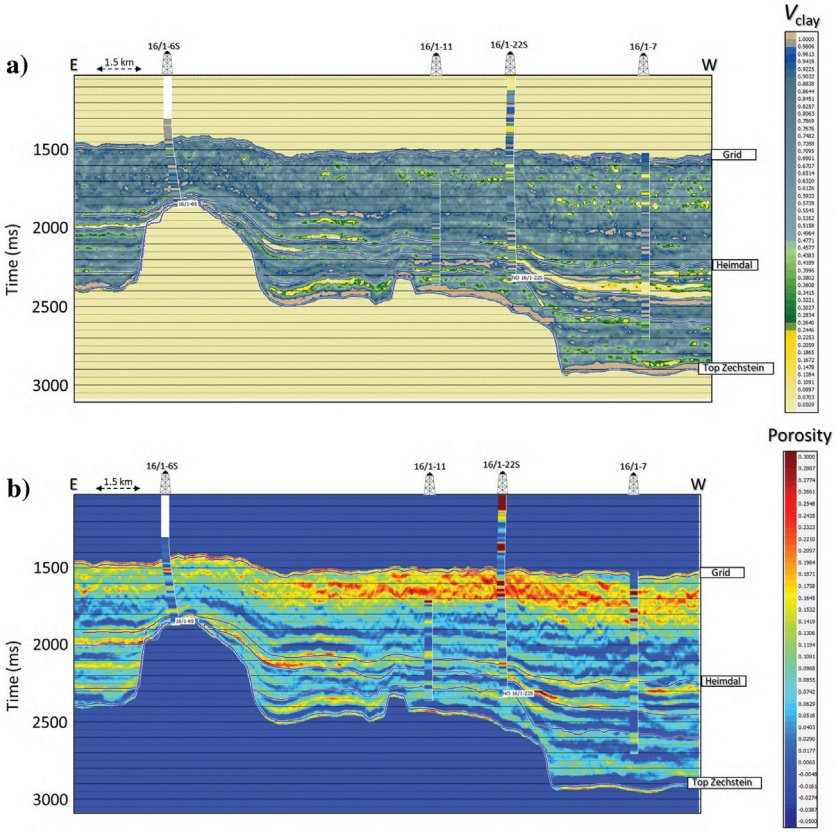

Figure 16. An arbitrary line section extracted from the (a) V_{clay} and (b) effective porosity volumes predicted using multiattribute analysis (data courtesy of TGS and AGS, Norway).

relative acoustic impedance; the P-impedance and S-impedance obtained from simultaneous impedance inversion; and the derived attributes such as lambda-rho, mu-rho, and Poisson's ratio volumes. Using the available wells and the input attributes, the optimal number of attributes and the operator length were selected using a cross-validation criterion as described earlier. An operator length of five samples exhibited a minimum validation error with four attributes. These attributes were the P-impedance, S-impedance, Poisson's ratio, and mu-rho. The correlation between the computed V_{clay} curve and the predicted curve was 86%.

After training, the validation process was followed, which showed a correlation of 80% at the well locations. A representative arbitrary line section from the predicted V_{clay} volume and passing through four wells is shown in Figure 16a. The computed V_{clay} curves based on petrophysical analysis are inserted in the display as a variable color log. A good match is seen, which enhances our confidence in the analysis. A lateral variation of V_{clay} is noticed in different intervals of interest.

A similar analysis was carried out for computation of the effective porosity volume. Figure 16b shows the display from the porosity volume equivalent to the arbitrary line display from the V_{clay} volume shown in Figure 16a. Again, a reasonable match between the inverted porosity and the inserted well-log curve computed based on petrophysical analysis is noticed, which is encouraging. A representative crossplot from the predicted V_{clay} and porosity volumes along an arbitrary line that passes through different wells is shown in Figure 17. The crossplot in Figure 17a is from the four wells shown on arbitrary line displays over our broad zone of interest and color coded with V_{clay}. An equivalent crossplot from the multiattribute analysis is shown in Figure 17b. A striking similarity is seen between the two crossplots, which lends confidence in the approach that has been used.

Moreover, on examining these two volumes simultaneously, we can differentiate between tight carbonate, shale, and high-porosity sand. To map these facies spatially at different levels, horizon slice displays from these two volumes close to the Heimdal and Draupne levels are shown in Figures 18 and 19, respectively. On these displays, the low values of V_{clay} (the yellowish color) might be associated with tight or porous sand as well as carbonate. However, consideration of the porosity volume along with V_{clay} makes it possible to differentiate among different facies. For example, if we consider the V_{clay} map shown in Figure 19a, we can track non-

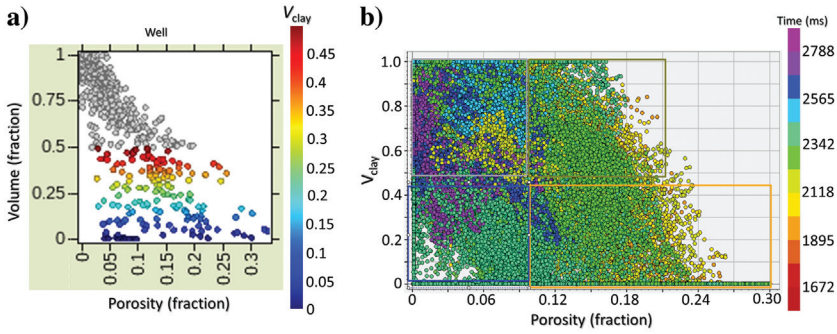

Figure 17. (a) Crossplot of V_{clay} versus porosity for well data (number of wells 4) over the zone of interest color coded with V_{clay}. (b) Equivalent crossplot generated from the computed petrophysical volumes. A striking similarity between the two crossplots lends confidence in the inverted attributes (data courtesy of TGS and AGS, Norway).

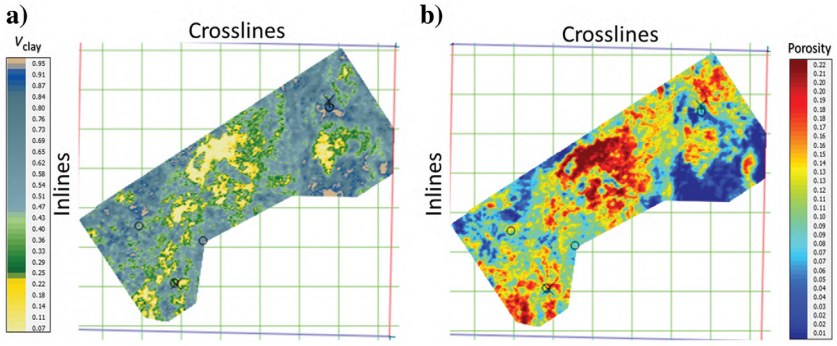

Figure 18. Horizon slices from (a) V_{clay} and (b) porosity volumes averaged over a 15 ms window above the Heimdal horizon (data courtesy of TGS and AGS, Norway).

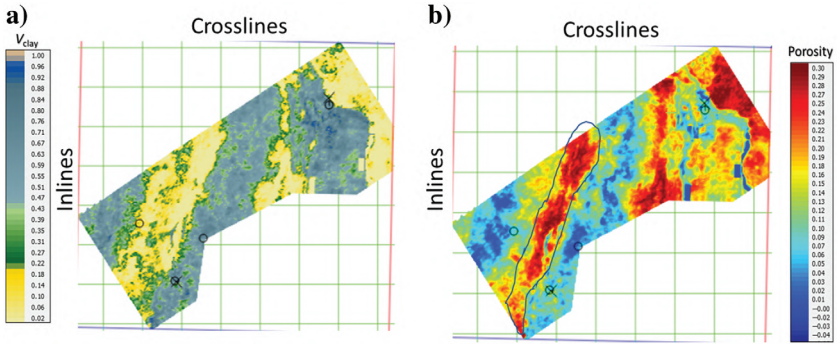

Figure 19. Horizon slices from (a) V_{clay} and (b) porosity volumes averaged over a 20 ms window above the Draupne horizon (data courtesy of TGS and AGS, Norway).

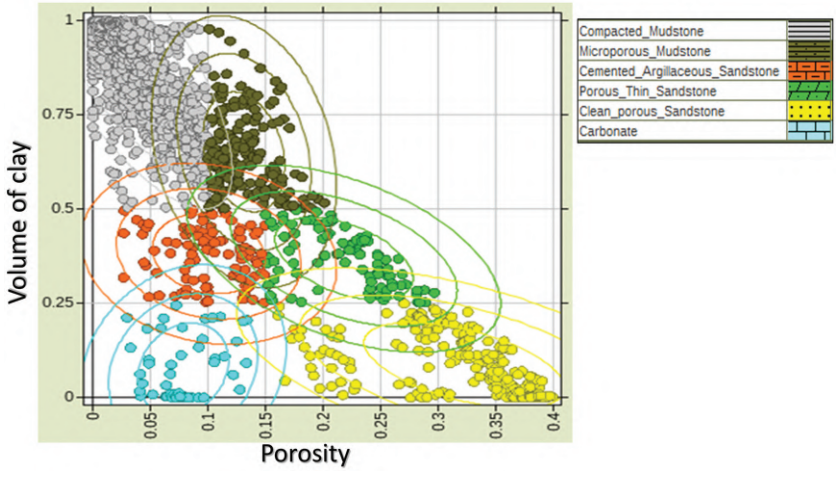

Figure 20. Interpretation of lithoclassification based on the well-log porosity and volume of clay of four wells by restricting their values. The probability density functions for the individual clusters are also shown overlaid.

shaly facies (sand/carbonate) by following the yellowish color. Furthermore, porous sand facies (highlighted with the blue polygon) can be differentiated from the adjacent tight carbonate facies when the porosity map is analyzed.

Facies determination using Bayesian classification

Instead of analyzing porosity and V_{clay} volumes simultaneously, a single facies volume can be generated by defining different cutoffs of these two volumes for the individual facies. For example, based on the high and low values of porosity and V_{clay}, respectively, four different facies can be defined in the crossplot space (Figure 17b). Needless to say, such an effort for defining different facies over our zone of interest using different polygons is subjective and can be updated with additional information. It is also possible that a wide range of values within each polygon may not represent the same facies. Understandably, the cluster points closer to the center within each polygon for the same facies should be more probable than the points away from the center. Consequently, an approach that accounts for the uncertainties associated with reservoir characterization in the different facies needs to be followed. One way of achieving this is with the application of the Bayesian classification approach, which yields a facies model reflecting the quality of the lithounits with a related uncertainty analysis.

With this information in mind, a fruitful discussion with a geologist and petrophysicist was carried out to define the different facies which make geologic sense based on the cutoffs of porosity and V_{clay}. The interpretation of these different updated restricted-value polygons is exhibited in Figure 20 in terms of their lithoclassification as seen on the legend in the inset. The probability density functions for these individual clusters were generated using Gaussian ellipses (Do, 2008) and are also shown overlaid in different colors. Based on all of this, the interpretation of the lithocolumns for the different wells is shown in Figure 21.

To gain confidence in the interpreted lithocolumns, they were compared to the facies classification that was defined by the petrophysicist independently, based on the computed individual mineral constituents and porosity for the four wells (16/1-7, 16/1-22S, 16/1-11, and 16/1-6S). A representative correlation of the generated facies with the interpreted lithology for well 16/1-7 is also shown in Figure 21 (left track), which seems to match reasonably well (sandstone in the Grid and Heimdal Formations, carbonate in the formation above Draupne, and shale in the Draupne Formation). Such a good correlation was found for the other wells also and lent confidence to our analysis.

As stated above, the probability distribution functions (PDFs) were generated from the Gaussian ellipses in Figure 20 and were used later for computing the facies from the inverted porosity, V_{clay} attributes. An arbitrary line

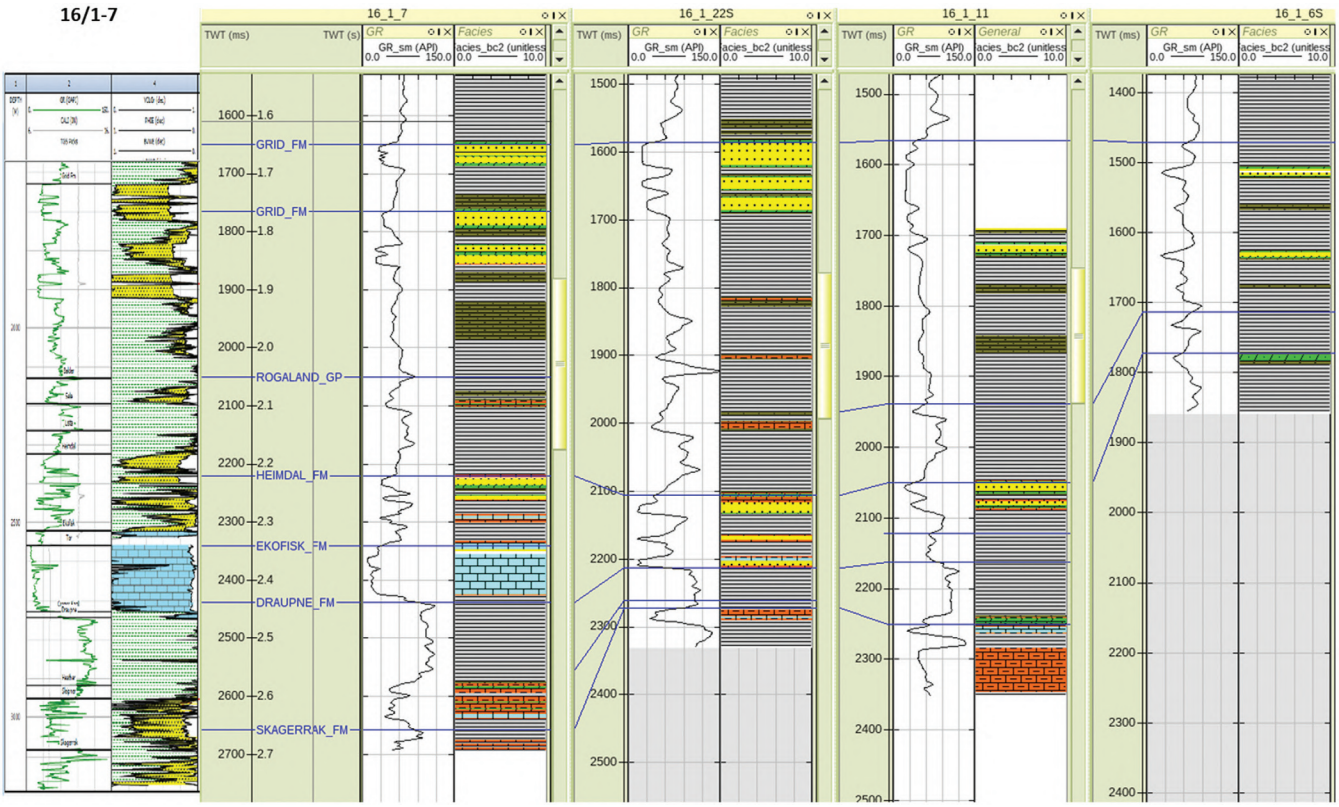

Figure 21. Interpretation of lithoclassification based on the V_{clay} and porosity curves on four wells. A representative correlation with the petrophysical interpretation for well 16/1-7 is also shown, which looks promising.

passing through the four wells and shown in the earlier displays was extracted from the generated facies volumes and shown in Figure 22. The Gamma-ray (GR) log curves are overlain on the display. This plot depicts useful facies information as indicated in the legend and that correlated well with the overlaid log curves. Note the existence of carbonate facies at the level of above the Draupne Formation in the eastern side of displayed section, which tend to match very well at the location of well 16/1-7. Similarly, clean, porous sandstone can be seen in the Heimdal Formation. The presence of thin, porous sand as well as microporous mudstone within the Grid Formation and compacted mudstone at the level of Draupne and above the Heimdal Formation makes geologic sense.

The probability of occurrence of different facies was also computed from the PDFs generated earlier, and the two equivalent arbitrary line displays are shown in Figure 23, for clean, porous sandstone facies (Figure 23a) and porous thin sandstones facies (Figure 23b). Although the red color shows a high probability of being a particular facies, the low probability is highlighted with the blue color.

Furthermore, to map the different facies spatially, the two stratal slices are shown in Figure 24, one 100 ms above the grid marker (Figure 24a) and the other 10 ms above the Heimdal marker (Figure 24b). The spatial distribution of the facies information seems convincing and matches the status of the wells overlaid on the displays at the respective levels. Such a facies distribution is

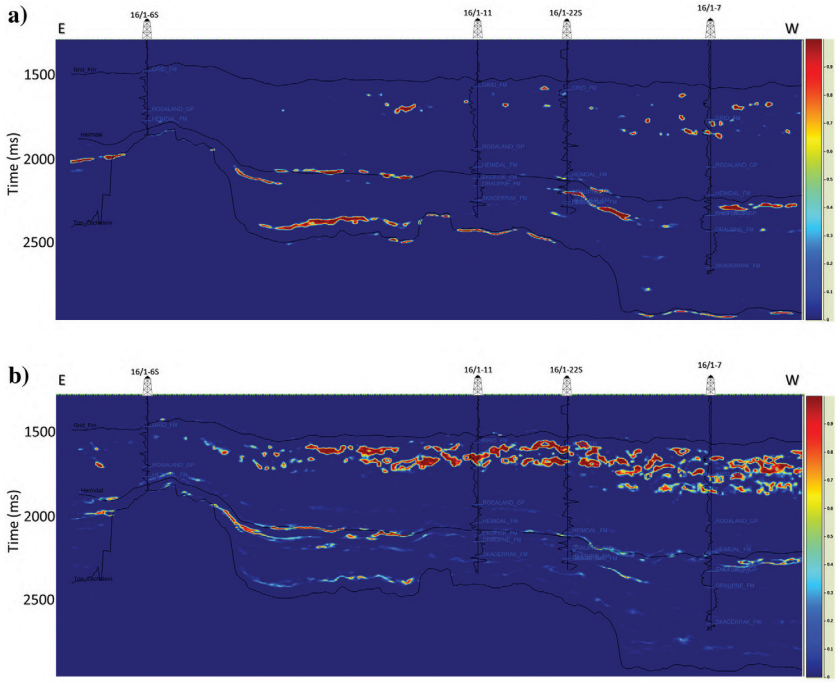

Figure 23. An arbitrary line section extracted from the maximum probability volume computed for (a) clean, porous sandstone and (b) porous, thin sandstone facies (data courtesy of TGS and AGS, Norway).

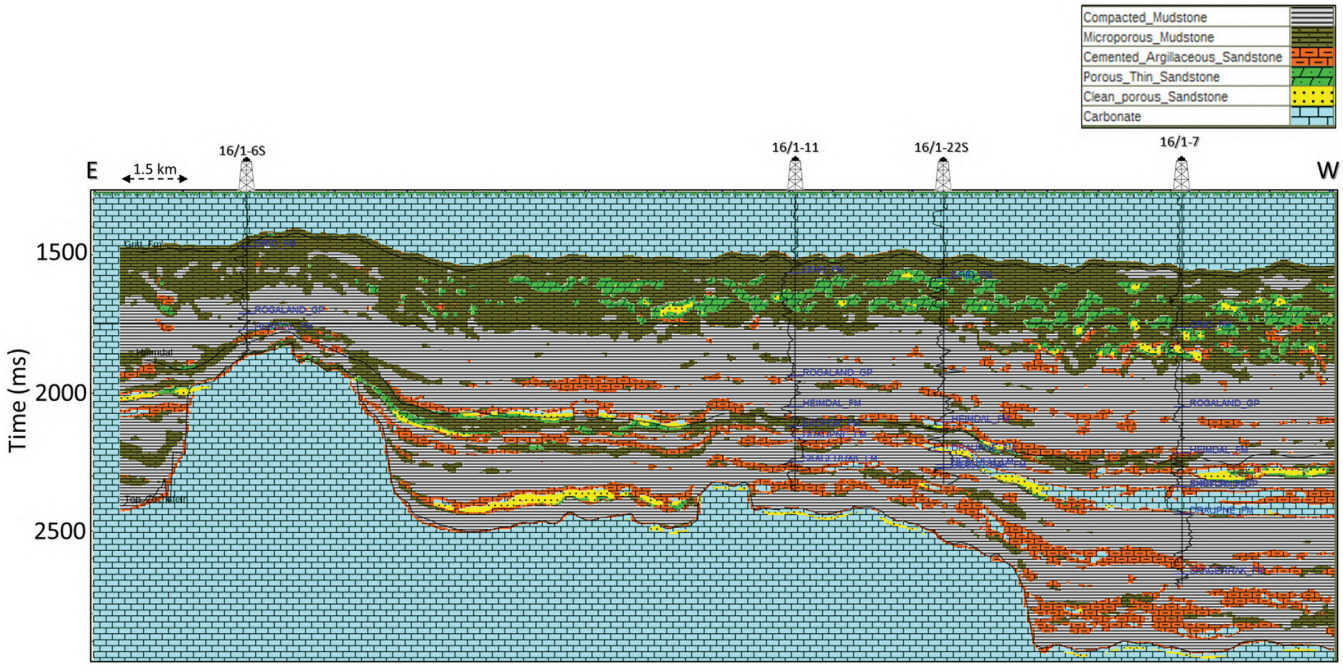

Figure 22. An arbitrary line section extracted from the facies volume generated from the inverted petrophysical attributes and the computed facies. The facies information in the different intervals seems to be much better refined that the information depicted on the equivalent section in Figure 20 (data courtesy of TGS and AGS, Norway).

Figure 24. Stratal slices extracted from the facies volume (a) 100 ms below the Top Grid marker and (b) 100 ms above the Top Heimdal (probable Heimdal) marker. The spatial distribution of the facies information seems convincing and matches the information available from the well data (data courtesy of TGS and AGS, Norway).

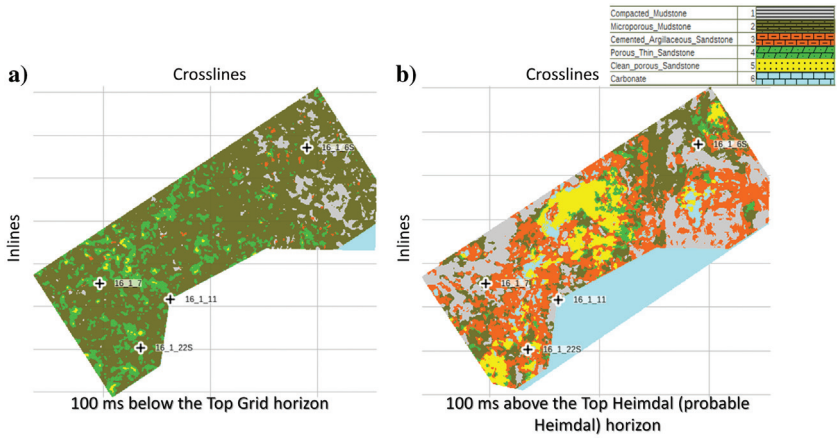

Figure 25. An arbitrary line section extracted from the water saturation volumes predicted using multiattribute analysis. A reasonable match is noticed between the predicted and overlaid well-log curves (data courtesy of TGS and AGS, Norway).

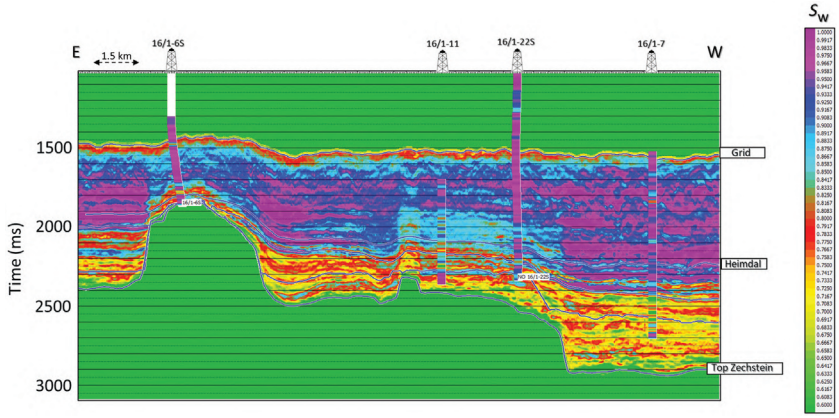

Figure 26. (a) Ten stratal slices generated between the Heimdal and Draupne markers shown on an inline section from the seismic data volume. Stratal slice displays close to the Draupne marker extracted from (b) V_{clay}, (c) porosity, and (d) water-saturation volumes. The lateral variation of the properties seen on these displays look promising (data courtesy of TGS and AGS, Norway).

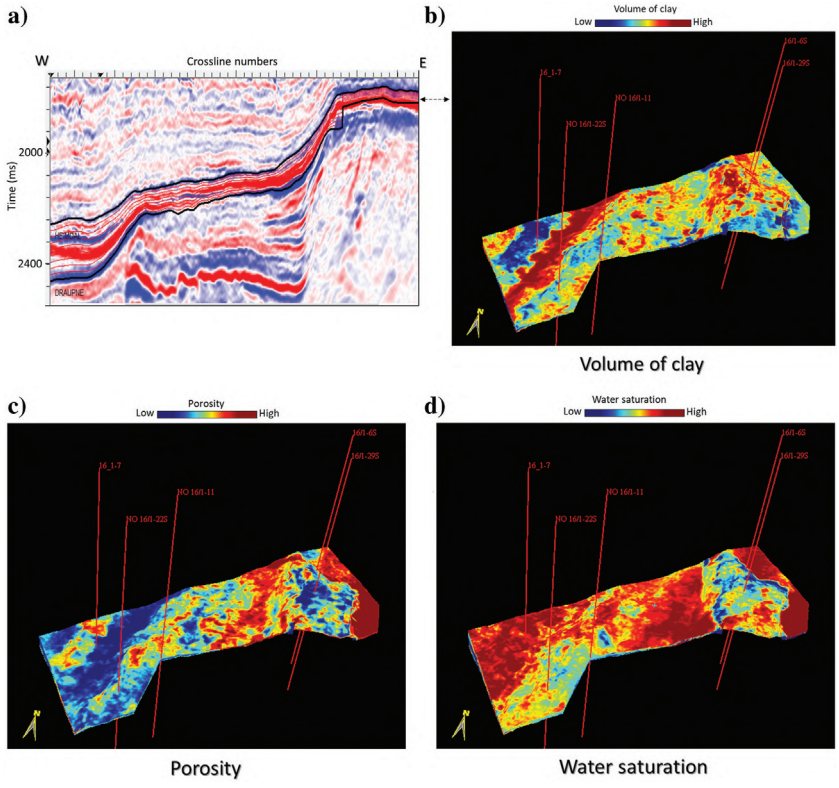

very helpful because it indicates the prospective zones that could be exploited at the different levels of interest by following the criteria of relatively low water saturation.

As mentioned earlier, the impact of water saturation on seismically derived attributes is not straightforward and needs to be analyzed for individual lithofacies. For doing so, the relatively low impedance or V_P/V_S along with other attributes within the individual lithofacies might be indicative of hydrocarbon-bearing pockets that could be picked up for more scrutiny and interpretation. Alternatively, multiattribute analysis can be followed to predict the water-saturation volume. Figure 25 shows the display from the water-saturation volume equivalent to the arbitrary line displays from the V_{clay} and porosity volumes shown in Figure 16a and 16b. A reasonable match between the predicted water saturation and inserted well-log curves is noticed, which is, again, encouraging. Having the water-saturation volume, it can be used along with the lithofacies volume or the V_{clay} and porosity volumes.

In Figure 26, we show the stratal displays in 3D perspective mode at a level just above the Draupne marker from the V_{clay} (Figure 26a), effective porosity (Figure 26b), and water saturation (Figure 26c) computed/inverted volumes. The lateral variation of the properties seen on these displays look promising. The facies and the petrophysical attribute volumes generated from seismic data when interpreted carefully will prove useful for the location of future wells to be drilled in the area.

Conclusion

The application of prestack simultaneous impedance inversion on the available seismic data volume over the Utsira High yielded useful attributes (P-impedance and S-impedance). We attempted to estimate the petrophysical parameters (the volume of shale, porosity, and water saturation) from them using extended elastic impedance. This method did not yield encouraging results; thus, we turned to our backup plan of using multiattribute regression analysis to generate petrophysical properties for the broad zone of interest comprising different lithointervals. This analysis was coupled with a Bayesian classification approach, which provided a workflow for defining different facies in the intervals of interest, and the results look promising. The integrated interpretation of these facies attributes as well as the petrophysical property data volumes are expected to be a valuable aid for future drilling in the area.

Acknowledgments

We wish to thank TGS for encouraging this work and for the permission to present and publish it.

Data and materials availability

Data associated with this research are confidential and cannot be released.

References

Chopra, S., and K. J. Marfurt, 2016, Spectral decomposition and spectral balancing of seismic data: The Leading Edge, **35**, 176–179, doi: 10.1190/tle35020176.1.

Chopra, S., R. K. Sharma, H. Nemati, and J. Keay, 2018, Seismic reservoir characterization of Utica-Point Pleasant Shale with efforts at quantitative interpretation — A case study — Part 1: Interpretation, **6**, no. 2, T313–T324, doi: 10.1190/INT-2017-0134.1.

Chopra, S., R. K. Sharma, A. K. Ray, H. Nemati, R. Morin, B. Schulte, and D. D'Amico, 2017, Seismic reservoir characterization of Duvernay shale with quantitative interpretation and induced seismicity considerations — A case study: Interpretation, **5**, no. 2, T187–T195, doi: 10.1190/INT-2016-0130.1.

Connolly, P., 1999, Elastic impedance: The Leading Edge, **18**, 438–452, doi: 10.1190/1.1438307.

Do, B. C., 2008, Lecture notes: The multivariate Gaussian distribution, http://cs229.stanford.edu/section/gaussians.pdf, accessed 30 May 2020.

Hampson, D. P., J. S. Schuelke, and J. A. Quirein, 2001, Use of multiattribute transforms to predict log properties from seismic data: Geophysics, **66**, 220–236, doi: 10.1190/1.1444899.

Isaksen, G. H., and K. H. I. Ledje, 2001, Source rock quality and hydrocarbon migration pathways within the greater Utsira High area, Viking Graben, Norwegian North Sea: AAPG Bulletin, **85**, 861–883, doi: 10.1306/8626CA23-173B-11D7-8645000102C1865D.

Leiphart, D. J., and B. S. Hart, 2001, Case history comparison of linear regression and a probabilistic neural network to predict porosity from 3-D seismic attributes in Lower Brushy Canyon channeled sandstones, southeast New Mexico: Geophysics, **66**, 1349–1358, doi: 10.1190/1.1487080.

Marfurt, K., and M. Matos, 2014, Am I blue? Finding the right (spectral) balance: AAPG Explorer, http://www.aapg.org/publications/news/explorer/column/articleid/9522/am-i-bluefinding-the-right-spectral-balance, accessed 12 September 2020.

Mukhopadhaya, P. K., and S. Mallick, 2011, An accurate ray-based offset-to-angle transform from normal moveout uncorrected multicomponent data in a transversely isotropic medium with vertical symmetry axis: Geophysics, **76**, no. 3, C41–C51, doi: 10.1190/1.3565182.

Ray, A. K., and S. Chopra, 2016, Building more robust low-frequency models for seismic impedance inversion: First Break, **34**, 29–34, doi: 10.3997/1365-2397.2016005.

Walden, A. T., 1991, Making AVO sections more robust: Geophysical Prospecting, **39**, 915–942, doi: 10.1111/j.1365-2478.1991.tb00350.x.

Whitcombe, D. N., P. A. Connolly, R. L. Reagan, and T. C. Redshaw, 2002, Extended elastic impedance for fluid and lithology prediction: Geophysics, **67**, 63–67, doi: 10.1190/1.1451337.

Zeigler, P. A., 1988, Evolution of the Arctic-North Atlantic and the Western Tethys: AAPG Memoir, **43**, 198.